

Geo-Congress 2026

GSP 379

Site Characterization, Rock Mechanics, and Unsaturated Soils

Selected Papers from Geo-Congress 2026
Salt Lake City, Utah | March 9–12, 2026

Edited by

Jack Montgomery, Ph.D., P.E.
Brady R. Cox, Ph.D., P.E.

ASCE

G-I GEO-INSTITUTE ASCE

GEOTECHNICAL SPECIAL PUBLICATION NO. 379

GEO-CONGRESS 2026

SITE CHARACTERIZATION, ROCK MECHANICS, AND UNSATURATED SOILS

SELECTED PAPERS FROM SESSIONS OF GEO-CONGRESS 2026

March 9–12, 2026
Salt Lake City, Utah

SPONSORED BY

The Geo-Institute
of the American Society of Civil Engineers

EDITED BY
Jack Montgomery, Ph.D., P.E.
Brady R. Cox, Ph.D., P.E.

Published by the American Society of Civil Engineers

Published by American Society of Civil Engineers
1801 Alexander Bell Drive
Reston, Virginia, 20191-4382
www.asce.org/publications | ascelibrary.org

Any statements expressed in these materials are those of the individual authors and do not necessarily represent the views of ASCE, which takes no responsibility for any statement made herein. No reference made in this publication to any specific method, product, process, or service constitutes or implies an endorsement, recommendation, or warranty thereof by ASCE. The materials are for general information only and do not represent a standard of ASCE, nor are they intended as a reference in purchase specifications, contracts, regulations, statutes, or any other legal document. ASCE makes no representation or warranty of any kind, whether express or implied, concerning the accuracy, completeness, suitability, or utility of any information, apparatus, product, or process discussed in this publication, and assumes no liability therefor. The information contained in these materials should not be used without first securing competent advice with respect to its suitability for any general or specific application. Anyone utilizing such information assumes all liability arising from such use, including but not limited to infringement of any patent or patents.

ASCE and American Society of Civil Engineers—Registered in U.S. Patent and Trademark Office.

Photocopies and permissions. Permission to photocopy or reproduce material from ASCE publications can be requested by sending an e-mail to permissions@asce.org or by locating a title in ASCE's Civil Engineering Database (http://cedb.asce.org) or ASCE Library (http://ascelibrary.org) and using the "Permissions" link.

Errata: **Errata, if any, can be found at https://doi.org/10.1061/9780784486740**

Copyright © 2026 by the American Society of Civil Engineers.
All Rights Reserved.
ISBN 978-0-7844-8674-0 (PDF)
Manufactured in the United States of America.

Preface

This is the fifth volume of seven Geotechnical Special Publications (GSPs) containing papers from Geo-Congress 2026: Geo Tools, Technologies, and Techniques in an Environment of Change, held in Salt Lake City, Utah, on March 9-12, 2026. Notably, this conference marks the 30th anniversary of the Geo-Institute. The conference brought together industry leaders, researchers, and practitioners to showcase innovations, address critical challenges, and advance knowledge in geotechnical engineering. The conference hosted the Terzaghi, Peck, Seed, and Prakash Lectures and many technical sessions, panel sessions, short courses, and student competitions.

These proceedings represent the culmination of nearly two years of effort by the program committee and many other individuals, whose focus has been to continue the success of previous Geo-Congresses and to celebrate 30 years of geotechnical innovation by the Geo-Institute. Building the program started with an international call for papers that resulted in more than 800 abstracts on a variety of important topics. Each paper was subjected to a rigorous technical review by two or more independent peer reviewers. Acceptance required concurrence by at least two peer reviewers, and final decisions were made only after review coordinators confirmed that authors satisfactorily addressed any reviewer comments on their original submission. All accepted papers are presented at the conference as posters or technical talks and are eligible for applicable ASCE awards.

This volume contains a collection of 56 papers focused primarily on the topics of engineering geology, site characterization, geophysical engineering, rock mechanics, and unsaturated soils. This includes papers on in-situ testing, machine learning and data-driven techniques, and non-invasive characterization and monitoring approaches.

The success of this conference and proceedings would not have been possible without the participation and collaboration of many individuals, including Brad Keelor, the tireless staff at the Geo-Institute, and the many session chairs and reviewers. We hope that these proceedings will be of use to the geotechnical engineering community for many years to come.

The Editors,

Jack Montgomery, Ph.D., P.E., M.ASCE, Auburn University
Brady R. Cox, Ph.D., P.E., M.ASCE, Utah State University

© ASCE

Acknowledgments

We are very grateful for the contributions of the authors, peer reviewers, session chairs, and program committee, without whom this publication would not be possible.

Geo-Congress 2026 Conference Program Committee

Conference Chairs
K. N. Gunalan, Ph.D., P.E., BC.GE, Pres. 20 ASCE, NAC, HNTB Corporation
Ryan B. Maw, P.E., G.E., BC.GE, F.ASCE, Gerhart Cole

Technical Chair
Shideh Dashti, Ph.D., M.ASCE, University of Colorado Boulder

Proceedings Editors
Brady R. Cox, Ph.D., P.E., M.ASCE, Utah State University
Jack Montgomery, Ph.D., P.E., M.ASCE, Auburn University

Student Program Liaison
Cassandra Rutherford, Ph.D., P.E., M.ASCE, Iowa State University

Program Committee Members
Aaron L. Leopold, P.E., M.ASCE, Dan Brown and Associates
Kam Ng, Ph.D., P.E., M.ASCE, University of Wyoming
Jenny Ramirez, Ph.D., P.E., M.ASCE, Geosyntec Consultants

© ASCE

Contents

Engineering Geology and Site Characterization

A Cone-Penetration-Test Inversion Model Trained by Machine Learning 1
Gunjan Rateria and Brett W. Maurer

A Hybrid Physics-Guided and Machine-Learning Framework for Modeling Ground Subsidence in the Greater Houston Area.....10
Yong Je Kim, Arip Syaripudin Nur, and Jinwoo An

Assessing the Spatial Variability in Geotechnical Sediment Properties on a Sandy Hardbottom Intertidal Beach.....20
Stephen Adusei, Nina Stark, Noah Evans, Jaquline Mueller, and Arianna Martin

Characterizing the At-Rest Lateral Stress Coefficient in South Carolina Coastal Plain Quaternary Sands 30
Andrew Russell, Ronald D. Andrus, Ali Sedaghat, Akhter Hossain, and Bikram Paudel

Cone Penetration Rate Effects on Field Characterization of Hydraulically Placed Fly Ash 41
Longde Jin, Andrew Fuggle, and Lina-Maria Pua Pita

Correlation between Monitoring While Drilling (MWD) Compound Parameters and Undrained Shear Strength of Fine-Grained Soils in Nebraska.....51
Michael Erzuah, Yasaman Abdolvand, Mohammadhossein Sadeghiamirshahidi, Nikolas Glennie, Alex Silvey, and Raul Velasquez

Development of Machine Learning-Based Software for Geotechnical Subsurface Characterization: Case Studies from Singapore 59
Ze Zhou Wang, Xiangfeng Guo, and Yue Hu

Drive Point Tests and Measurement-While-Drilling Technologies: Literature Review 70
Syed Shadman Sakib, Jie Han, and Robert L. Parsons

Enhancing 3D Soil Characterization through Machine Learning from CPT Data 81
Laith Sadik and Sara Khoshnevisan

Enhancing Geotechnical Data Workflows through Open-Source Integration 91
Xin Peng and Jesse G. Rauser

© ASCE

Evaluating Time-Dependent Strength Gain in Tailings Using Cone Penetration Test Data from a Large Tailings Storage Facility.....102
Akhter Hossain, Juan Carlos Ayes-Zamudio, and Tony J. Freiman

Experimental Investigation of the Depth of Influence of Simultaneously Recorded Compactometer and Machine Drive Power Measurements.....111
William J. Baker III and Christopher L. Meehan

Exploring the Potential of Nuclear Magnetic Resonance (NMR) for Geotechnical Property Characterization.....121
Ryan A. Rasanen

Exploring UAV Survey for Geotechnical Applications: A Comparative Study of Photo and Video Capture Techniques.....132
Mohammadamin Nozari, Siamak Yoosefi, Mohammadreza Jebeli, William J. Baker III, and Christopher L. Meehan

These pages intentionally left blank.....144

Machine Learning-Based Estimation of SPT-N Values from CPT Measurements.....152
Vahidreza Mahmoudabadi and Milad Fatehnia

Measurement of Soil Thermal Conductivity Using a Novel CPTu Module: An Update.....163
Joseph Bindner, Ong Siau-Hwa, and Ethan Cargill

Meshless Numerical Modeling of Vane Shear Test.....171
Alomir H. Favero Neto, Gustavo R. A. Oliveira, and Alfonso Cerna-Diaz

On the Use of CPT Correlations to Identify and Determine the Engineering Properties of Diatomaceous Soils.....181
Ariadna Covarrubias Ornelas, Diane Moug, and T. Matthew Evans

Seismic Geotechnical Imaging Using Full-Waveform Inversion and Physics-Informed Neural Networks.....191
Yuze Pu and Kami Mohammadi

Site Characterization Using Electrical Resistivity Tomography after Microbially Induced Desaturation Treatment.....201
Andres F. Cordoba-Ordonez, Aaron P. Gallant, Diane M. Moug, Kayla R. Sorenson, Arash Khosravifar, Leon A. Van Paassen, Luis E. Zambrano-Cruzatty, and Fadzai Zivanai

Sustained Collapse Testing of Soluble Soils in the Moab Valley.....211
Taylor Quinn Hall

© ASCE

Undrained Shear Strength from CPTU in Soft Clay, Stiff Till, and Soft Rock in the UK 220
Paul W. Mayne

Using Machine Learning (ML) Method to Improve Correlations between SPT and TCP Data 228
Jie Huang, Drew Johnson, and Fei Wang

Validating Machine Learning Based Subsurface Predictions with Geophysical and Boring Data 238
Aavash Ghimire, Kaleigh M. Yost, Ross Cutts, and Tieyuan Zhu

Verification Infiltration Testing for the Stormwater Management Design for a Light Rail Extension Project in Washington State 249
Roy Jensen, Blake Lytle-Goldstein, William Hickey, Madan Karkee, and Garry Horvitz

Water Adsorption of Non-Saline and Salt-Affected Clay 258
Shaya Banar and Omid Ghasemi Fare

Geophysical Engineering

Acoustic Emissions Monitoring of Cohesive and Cohesionless Soils during Consolidation and Shear Phases 267
Saad Allah Solh and Sherif L. Abdelaziz

Feasibility of Slope Failure Identification Using Google Street View 277
Tingkai Wang, Justine Talia Gacho, Benamar Mebarkia, Daniel Gao, and Xinbao Yu

Geotechnical Engineering and Near-Surface Geophysics—Correlations of Parameters Using Machine Learning 288
David J. Barrick and Curtis A. Link

Imaging Suspended Sediment Concentration in Ship Channels with Marine Electrical Resistivity 298
Andrew Gombac, Stacey Kulesza, and Jens Figlus

Improved Correlations of Geophysical Models with Sparse Borehole Data Using Geostatistical Algorithms 309
Alastair McClymont and Eric Johnson

Leveraging Advances in Passive Seismic Methods for Improved Ground Risk Management from Project Planning to Construction 321
Thaleia Travasarou, David Valintine, and Gouri Mohan

© ASCE

Machine Learning-Based Prediction of Soil Electrical Resistivity Using Field-Instrumented Hydrologic Data **332**
Md. Jobair Bin Alam, Robi Sonkor Mozumder, Chukwuzubelu Okenwa Ufodike, and Naima Rahman

Monitoring Soil Resistivity in Highway Slopes Stabilized with Vetiver Grass **343**
Fariha Rahman, Sadik Khan, and Avipriyo Chakraborty

Rapid Three-Dimensional Subsurface Imaging with Data-Driven Full Waveform Inversion **351**
Samuel Nakai, Sanish Bhochhibhoya, and Joseph P. Vantassel

Seismic Full Waveform Inversion for Sinkhole Assessment and Remediation Monitoring: A Case Study on a Roadway in Montgomery County, Pennsylvania **361**
Pourya Alidoust, Joseph T. Coe, Sarah McInnes, and Katherine Kubiak

Surface Effects on Variability of Horizontal-to-Vertical Spectral Ratio (HVSR) Measurements in Urban Areas **370**
Braydon Smith and Brent L. Rosenblad

Rock Mechanics

Dynamic Stability Assessment of a Jointed Rock Slope in the Seismically Active Himalayan Region: A Case Study from Uttarakhand, India **380**
Amalesh Jana, Arindam Dey, and Sreedeep S

Effect of Dual Surface Cracks on the Seismic Stability of Strip Footing Placed over Rock Mass **392**
Avneet Lahariya and Debarghya Chakraborty

Evaluation of Flexure Modulus and Energy Dissipation in Intact Rocks Using Resonant Column Testing and Numerical Simulations **404**
Sakshi Rohilla, Resmi Sebastian, and Arghya Das

Evaluation of Rock Fractures in the Laboratory Using Acoustic Emissions Measurements and Digital Image Correlation **416**
Shivesh Shandilaya and Shahrzad Roshankhah

Potential of Biopolymer-Enhanced EICP Biocementation in Rock Mass **427**
Mary C. Ngoma and Oladoyin Kolawole

Recommendations for Selecting an Optimal Rock Joint Direct Shear Test Procedure **435**
Steve Berry and Mary MacLaughlin

© ASCE

Unsaturated Soils

A Coupled Thermo-Hydraulic Transfer Model for Soil Freezing 446
Antai Dong and Xiong Zhang

Assessing the Impact of Wildfire Intensity on Soil Hydrology and Stability: The Role of Soil Organic Matter and Mulching Strategies.....455
Avishek Ghosh, Md. Raihanul A. Chowdhury, and Aritra Banerjee

Biopolymer-Based Injection into Cracked Soil Mass: Evaluation of Workability, Shrinkage, and Bonding Performance 466
Leela Krishna Mohan, Zachary Nick, Samantha Lucker, Lucas Walshire, and Marcelo Sanchez

Data-Driven Parameterization and Comparison of SWCC Models 477
Robi Sonkor Mozumder, Fyaz Nafin Rahman, Md. Jobair Bin Alam, and Naima Rahman

Effective Stress Evaluation of the Thermal Volume Change of Swelling Soils.....488
Xufei Liu, Fatemah Behbehanhi, Yu Lu, and John S. McCartney

Integrating Numerical Modeling and Stochastic Weather Generation to Predict Environmentally Driven Seasonal Ground Movements in Expansive Clays 499
Mahdi Seyyedan, Jiali Ma, and Andrew J. Whittle

IoT-Enabled Data-Driven ML for Predictive Modeling in Unsaturated Soil Mechanics.....509
A. Q. M. Zohuruzzaman, Mahdi Zulfikar, and Sadik Khan

Contact Angle Measurement of Soil Minerals by Sessile Drop (SD) and Water Drop Penetration Time (WDPT) Methods 519
Ali Behdad, Yuan Feng, Laith Ibdah, and Jongwan Eun

Nonlinear Shear Strength Characteristics of a Silty Soil under Varying Moisture Conditions 529
Kalani Rajamanthri, Sravan Kumar Thandrangi, and Claudia E. Zapata

Numerical Analysis of Thermo-Hydro-Mechanical Behavior of Expansive Soils Close to Geothermal Energy Systems 539
Fereydoun Najafian Jazi, Kiarash Jafarzadeh Marandi, Omid Ghasemi-Fare, and Thomas D. Rockaway

© ASCE

Probabilistic Analysis of Compacted Embankments Using Kriging Surrogates **550**
Rakshanda Showkat, G. L. Sivakumar Babu, and Deepankar Choudhury

Seismic Fragility of Buried Pipelines following Pluvial Events **560**
Ali Shojaeian, Tommy Bounds, and Kanthasamy K. Muraleetharan

© ASCE

A Cone-Penetration-Test Inversion Model Trained by Machine Learning

Gunjan Rateria, S.M.ASCE[1]; and Brett W. Maurer, M.ASCE[2]

[1]Graduate Research Assistant, Dept. of Civil and Environmental Engineering, Univ. of Washington, Seattle, WA. Email: gun1705@uw.edu
[2]Associate Professor, Dept. of Civil and Environmental Engineering, Univ. of Washington, Seattle, WA. Email: bwmaurer@uw.edu

ABSTRACT

Volume-averaging effects significantly impact the accuracy of cone penetration test (CPT) measurements in layered soil profiles. This study introduces a machine learning (ML)-based inversion model designed to correct these effects, trained on an extensive dataset that combines results from existing literature and new virtual calibration chamber experiments using the discrete element method. The inversion model achieves a mean absolute percentage error of 13% on unseen data, outperforming existing methods to a statistically significant degree. Its limitations include: (1) reduced accuracy in very thin layers and in conditions beyond the training set's parameter space; (2) interpretability challenges typical of ML-based approaches; and (3) uncertainties inherent to virtual methods' abilities to represent physical reality. Despite these limitations, this study demonstrates the feasibility of a novel approach to developing CPT inversion models and results in an easy-to-use model that warrants adoption and further scrutiny.

INTRODUCTION

The CPT is widely used for subsurface characterization and hazard assessment, but its measurements are inherently blurred by the soil volume mobilized during penetration. This "volume-averaging" effect, which depends on soil stiffness and cone size, filters out high-frequency stratigraphic details, often distorting true values of cone resistance (q_c) and sleeve friction (f_s). While negligible in thick homogeneous soils, this effect can significantly obfuscate interpretations in layered profiles, leading to errors in liquefaction hazard assessment or foundation design, where soil properties and behaviors are integrated over depth. These systematic distortions underscore the need to correct volume-averaging effects in CPT data, especially in layered soils.

Limitations of Existing Models and Motivation for New Approach

Past efforts to address volume-averaging effects have included empirical correction charts and algorithmic models informed by limited physical or virtual calibration chamber (VCC) experiments. These efforts have led to inversion models that estimate true resistance profiles from measured CPT data. Early models, some of which are illustrated in Figure 1, were chart-based, while more recent algorithmic models (e.g., Boulanger and DeJong, 2018; De Greef & Lengkeek, 2018; Cooper et al., 2022) offered improved practicality. Still, these approaches were developed with very limited data, many of which suffer from scale effects, boundary artifacts, or insufficient layering complexity. There are few independent evaluations of any inversion model, and the results of these evaluations encourage further research and development (e.g., Yost et al.

© ASCE

2021; Geyin and Maurer 2021). Despite progress, existing models remain constrained by the quantity and quality of available training data, limiting their applicability across diverse conditions. Physical tests are costly and prone to material inconsistencies, while prior VCCs have rarely targeted volume-averaging effects explicitly. To overcome these limitations, this study compiles the largest known dataset of CPT responses in layered soils, including new 3D discrete element method (DEM) simulations. An ML framework is then trained to correct volume-averaging effect using only standard CPT inputs, enabling a practical, data-driven solution that improves on current models.

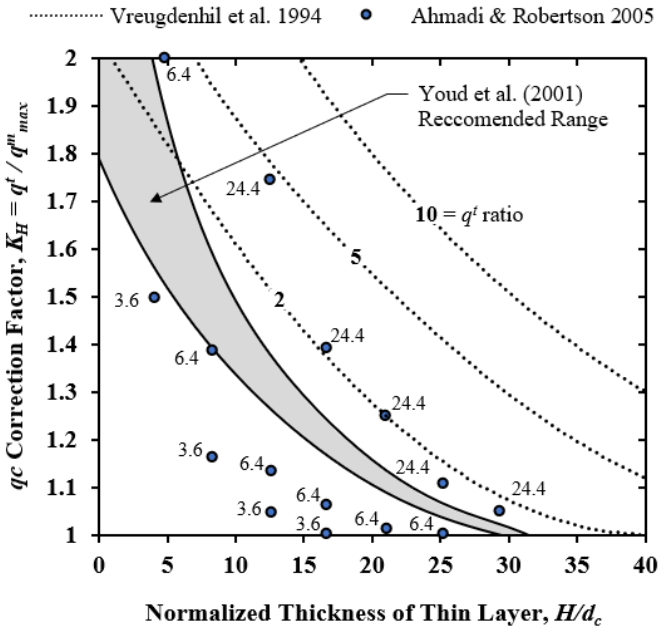


Figure 1. Example q_c correction factors for stronger strata interbedded in weaker strata; all data labels denote the ratio of q^t in the stronger strata to q^t in the weaker strata.

Data and Methodology:

A total of 179 VCC simulations were conducted using EDEM 2024.1 to generate paired measured (q^m) and true (q^t) CPT profiles in layered and homogeneous soils. Each simulation employed a 1-m diameter, 1-m tall chamber filled with ~1.5 million spherical particles (modal size = 3 mm), achieving a cone diameter (d_c) to mean particle size ratio of 12, larger than in most prior 3D VCC studies (e.g., Ciantia et al. 2016; Khosravi et al. 2020). Twelve distinct layers were pluviated under gravity, with the thinnest being 4 cm. This minimum thickness (~1.1d_c) was determined through a parametric study to be the practical resolution limit below which ML models tend to misinterpret particle-scale noise as layering. Friction was temporarily disabled during deposition to facilitate packing, and particles were graded by size (3–13.5 mm) to enhance contact stability and control measurement variance. Simulations were performed quasi-statically with a 10 cm² cone penetrating at 0.3 m/s under boundary stresses of 100 kPa (vertical) and 50 kPa (radial). The inertial number was kept $<10^{-2}$ to ensure quasi-static conditions. A time step of 6.8×10^{-6} s was selected to balance accuracy and computational cost. Four synthetic soils (A–D) were modeled using the Hertz-Mindlin no-slip contact law with rolling resistance to

© ASCE

replicate a range of shear strengths and compressibility. These properties were calibrated using DEM-based direct shear tests and are summarized in Figure 2 and Table 1. Material A has the least shear strength, lowest q_c, is most compressive, and has a soil behavior type index (I_c) (Robertson and Wride, 1998) consistent with clayey soil. Material D has the greatest shear strength, highest q_c, is most dilative, and has an I_c consistent with clean sand. The remaining two materials represent intermediate soils, with I_c values suggesting silty soil mixtures. VCC profiles featured up to four interbedded materials with layer thicknesses ranging from 4 to 50 cm.

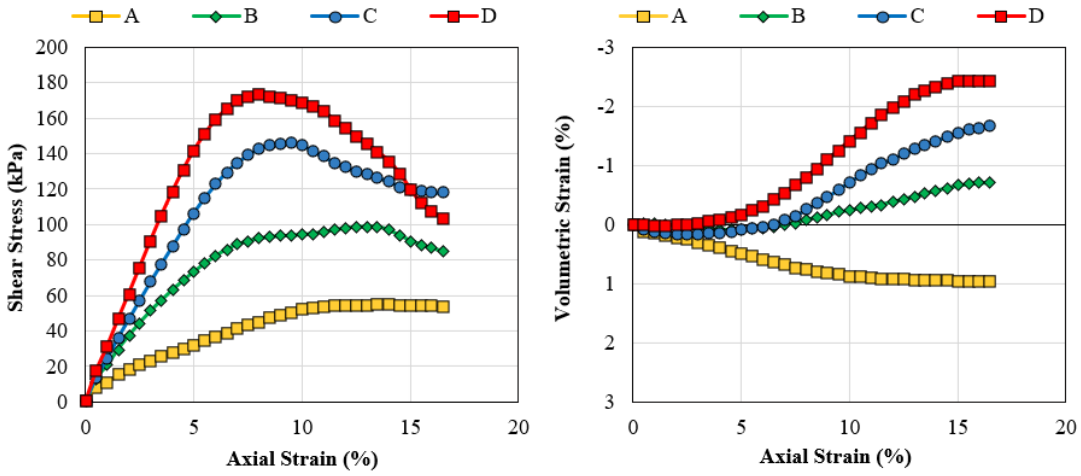


Figure 2. Simulated test results depicting the behaviors of materials A through D.

Table 1. Select micro and macro properties of materials A through D.

Material	Young's Modulus (MPa)	Coefficient of Restitution (COR)	Friction Coefficients				Cone tip Resistance q_c (MPa)	Soil Behavior Index I_c
			Particle-Particle		Cone-Particle			
			Static	Rolling	Static	Rolling		
A	15	0.3	0.2	0.05	0.2	0.05	0.5	3.18
B	75	0.6	0.25	0.4	0.25	0.35	1.5	2.62
C	100	0.75	0.6	0.45	0.35	0.35	3.7	2.15
D	150	0.95	0.8	0.5	0.4	0.375	5.7	1.91

To augment the VCC experiments conducted in this study, an additional 80 experiments were adopted from the literature, of which 41 were physical and 39 were virtual. Additionally, to improve early model performance and reduce false positives, 20 additional homogeneous VCC profiles were developed. Profiles with layers thinner than $1.1d_c$ were excluded, as they introduced noise difficult to distinguish from true volume-averaging effects. Literature data were excluded from model development if exhibiting large, unexplained deviations between q^m and q^t, suggestive of material or procedural inconsistencies.

The dataset was randomly split: 15% for testing and 85% for training. To reduce bias from internal data dominance (~75%), external data were upweighted 3X during training. Further resampling was performed to balance the representation of q^m/q^t ratios in the dataset, smoothing their distribution and encouraging physically consistent, monotonic model behavior.

© ASCE

VCC Results and Comparison with the Literature

Volume-averaging effects were analyzed using two parameters: the sensing distance (H_S), the depth above a material interface where the cone begins to sense the underlying layer, and the development distance (H_D), the depth below the interface where the cone fully responds to the new material (Figure 3). Stiffer materials exhibited larger H_S and H_D values due to greater volume mobilization, as illustrated in Figures 3 and 4. For instance, when material D (stiffer) overlies material A (weaker), $H_S \approx 4.5 d_c$. When reversed, H_S drops to $\approx 1 d_c$. These and other results align with prior experimental studies (e.g., Ahmadi and Robertson, 2005; Yost et al., 2022).

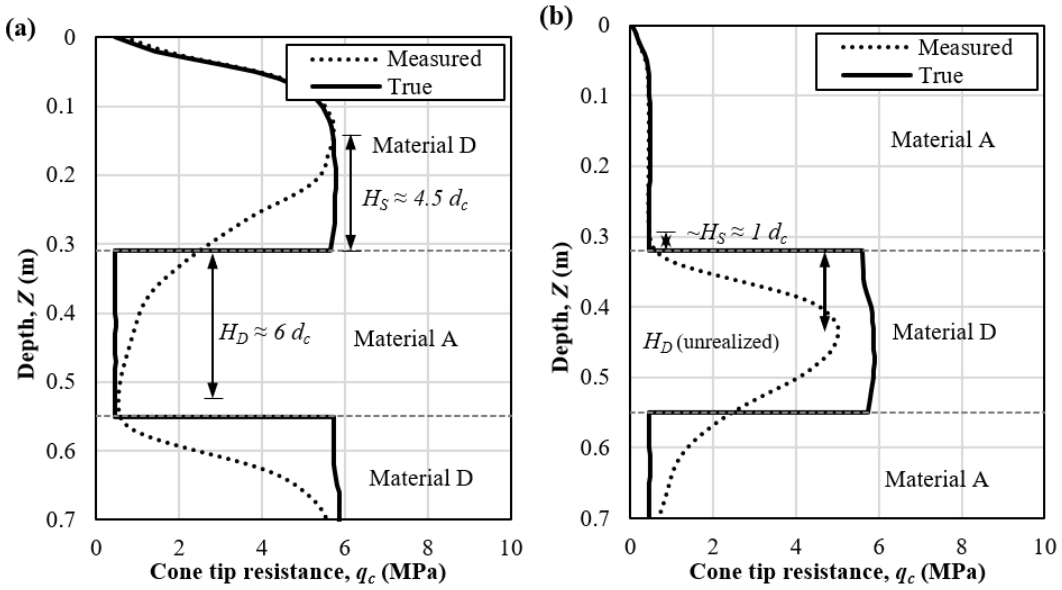


Figure 3. Example VCC results showing volume-averaging effects: (a) material A interbedded in material D; (b) material D interbedded in material A.

The observed q^m response was also influenced by asymmetric particle migration at interfaces. As shown in Figure 5, stiff-over-weak layering caused downward migration of stiff particles, delaying the full development of q^t. In contrast, weak-over-stiff layering tends to lead to minimal migration, allowing q^m to reach q^t more quickly.

Machine Learning Framework

An ML approach was adopted and addressed known limitations in prior geotechnical ML studies, such as insufficient cross-validation and lack of unbiased testing, lack of baseline comparisons, and limited practical usability (Maurer and Sanger, 2023). Over 2,000 features were initially extracted to describe fluctuations in q^m over spatial scales from 0.1 to 2.5 d_c, including normalized first and second derivatives. Eighteen predictors were ultimately selected based on variable importance, correlation structure, performance, and expert judgment. These are given in Table 2.

© ASCE

Multiple algorithms were explored including support vector machines, neural networks, and decision tree ensembles. Bagged decision trees were selected for their strong performance, low overfitting risk, and interpretability. Numerous model iterations were evaluated using different hyperparameters, feature sets, loss functions, and data-weighting strategies. The final model is made accessible to users through *ConeVersion*, a user-friendly Windows software.

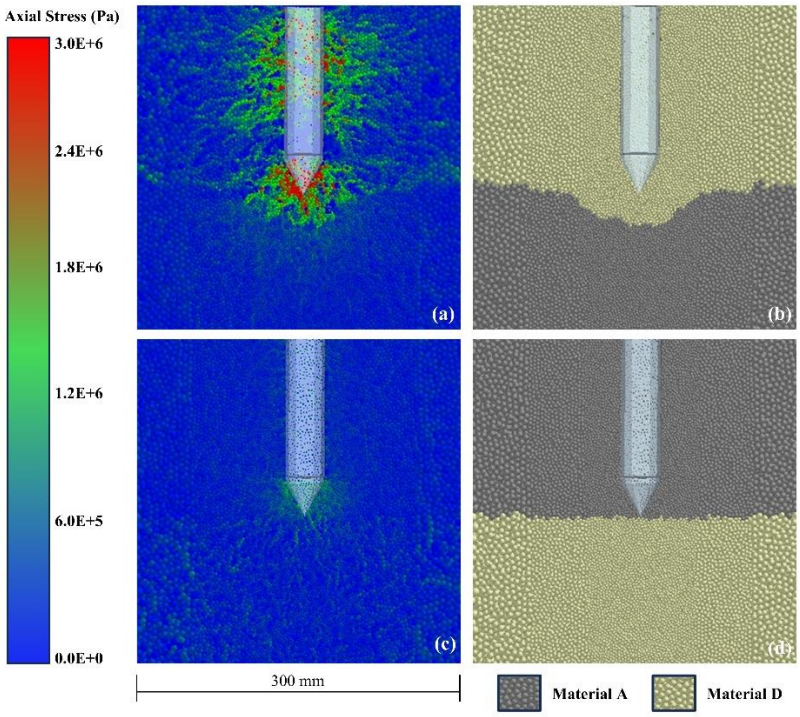


Figure 4. Example VCC results showing particle axial stresses and particle positions when: (a, b) material D overlies material A; (c, d) material A overlies material D.

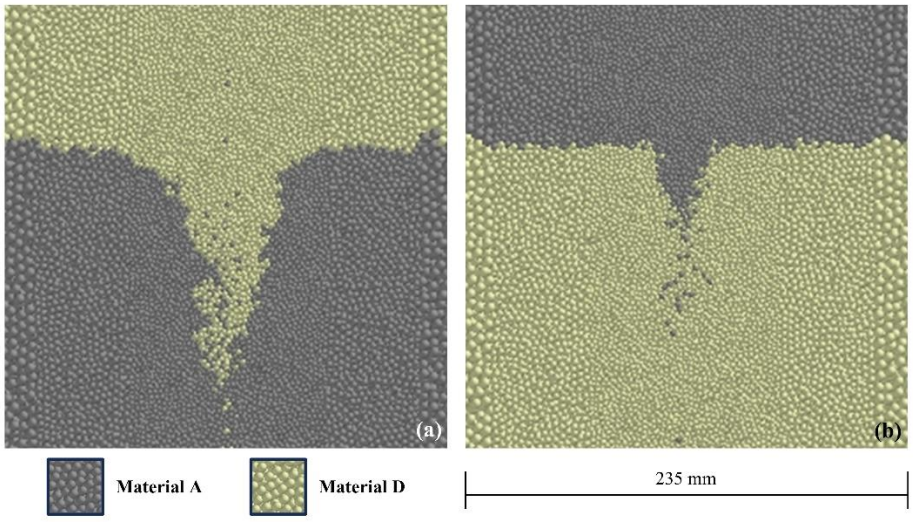


Figure 5. Example VCC results showing particle positions after penetration when: (a) material D overlies material A; and (b) material A overlies material D.

© ASCE

Table 2. Summary of 18 predictor variables adopted in final model.

Predictor	Numerical Representation (n = 1 : length (depth (Z))	Distance Intervals (x and y)
Forward first derivative of q^m w.r.t (Z/d_c) over distance x, normalized by q^m	$A_x = \frac{q^m(n+x)-q^m(n)}{q^m(n)*\left(\frac{x}{d_c}\right)}$	$x = 0.3d_c, 2d_c$
Central first derivative of q^m w.r.t (Z/d_c) over distance $2x$, normalized by q^m	$B_x = \frac{q^m(n+x)-q^m(n-x)}{q^m(n)*\left(\frac{2x}{d_c}\right)}$	$x = 0.9d_c$
Backward first derivative of q^m w.r.t (Z/d_c) over distance x, normalized by q^m	$C_x = \frac{q^m(n-x)-q^m(n)}{q^m(n)*\left(\frac{x}{d_c}\right)}$	$x = 2.5d_c$
Second forward derivative of A_x over distance y	$\frac{A_x(n+y)-A_x(n)}{\left(\frac{y}{d_c}\right)}$	$x =$, $y =$ $0.1d_c$, $1.4d_c$ $0.3d_c$, $1.5d_c$ $0.5d_c$, $1.9d_c$ $1.2d_c$, $0.4d_c$ $2.1d_c$, $0.8d_c$ $2.4d_c$, $0.2d_c$
Second central derivative of B_x over distance $2y$	$\frac{B_x(n+y)-B_x(n-y)}{\left(\frac{2y}{d_c}\right)}$	$x =$, $y =$ $0.5d_c$, $0.6d_c$ $1.4d_c$, $1.2d_c$ $1.7d_c$, $1.7d_c$
Second back derivative of C_x over distance y	$\frac{C_x(n-y)-C_x(n)}{\left(\frac{y}{d_c}\right)}$	$x =$, $y =$ $0.1d_c$, $0.4d_c$ $0.3d_c$, $1.3d_c$ $0.4d_c$, $2.5d_c$
Difference in A_x values	$A_{0.1d_c+x} - A_x$	$x = 0.9d_c$
Difference in C_x values	$C_{0.1d_c+x} - C_x$	$x = 0.9d_c$

RESULTS AND DISCUSSION

The ML model was tested on 3,075 CPT measurements not used in training. Here, the model prediction of q^t from q^m is compared to the actual, known q^t. Figure 6 compares predictions from: (i) the ML model; (ii) BD18 (Boulanger and DeJong, 2018 via CLiq); and (iii) DL18 (De Greef and Lengkeek, 2018 via CLiq). Since DL18 only permits upward correction ($q^t/q^m \geq 1.0$) and requires fs to compute Ic, it is inapplicable to CPTs lacking fs (e.g., Fig. 6d). Model performance for each profile is quantified via mean absolute percentage error (MAPE), given in the legends.

Several trends emerge. BD18 tends to overcorrect in homogeneous deposits by interpreting small-scale variability as volume-averaging effects (e.g., Fig. 6a). The ML model consistently achieves lower MAPEs, more accurately capturing both q^t values and material interfaces (e.g., Fig. 6b), but is susceptible to behaviors that depart from mechanistic sensibilities (e.g., Fig. 6d), highlighting its empirical nature. Future iterations could use mechanics-informed constraints.

© ASCE

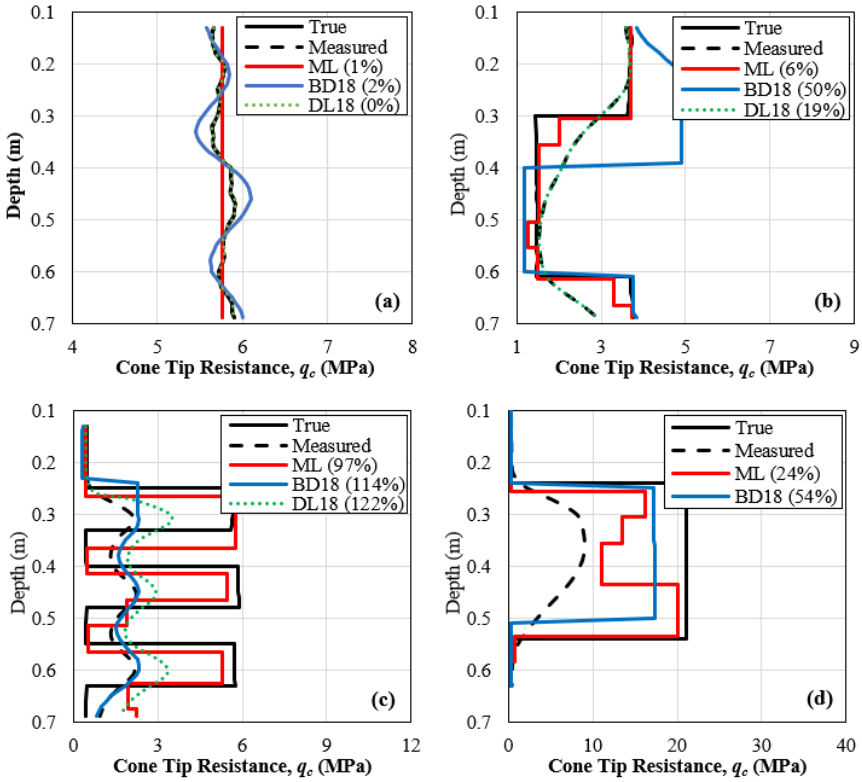


Figure 6. Example test profiles where the observed q^m and q^t are plotted against predictions of q^t made by three models (mean absolute percentage errors are given in the legend).

Table 3 summarizes overall performance. The ML model outperforms BD18 and DL18 with a test-set MAPE of 13%. Bootstrap sampling was used to compute 95% confidence intervals to reflect finite-sample uncertainty, confirming statistical significance of the performance gap. To assess broader trends, the models were also applied to two larger CPT datasets: (i) 5,668 CPTs from Canterbury, New Zealand (Geyin et al., 2021); and (ii) 332 CPTs from 25 global earthquakes (Rateria et al., 2024). Though *qt* is unknown, these datasets reveal behavioral differences. The ML model prescribes little or no correction for ~40% of CPTs, whereas BD18 does so for only ~5%. BD18 frequently applies large corrections (e.g., $q^t/q^m > 1.5$ in 20% of global cases), while the ML model is more restrained (8% > 1.5). These trends are also evident in Fig. 7(a). The ML model's q^t/q^m distribution aligns closely with its training data, underscoring its data-driven nature. Larger corrections in the global dataset may reflect its broader geologic diversity or finite-sample effects.

Table 3. Test set mean-absolute-percent-errors (MAPEs) and 95% confidence intervals.

Model	Mean Absolute Percent Error (MAPE)	95% CI on MAPE	
ML	13%	10%	15%
BD18	25%	23%	27%
DL18	32%	29%	35%

© ASCE

Despite promising performance, the ML model has limitations. Its accuracy and behavior are tightly linked to the training data, much of which was generated via VCC simulations. These materials were designed to span a range of shear strengths and compressibility, with physically plausible micro-properties, but cannot be assumed to represent true physical behavior. Achieving macro-scale realism through DEM calibration often results in non-unique micro-property combinations. While data from literature were upsampled to balance sources, a larger and more diverse dataset is desirable.

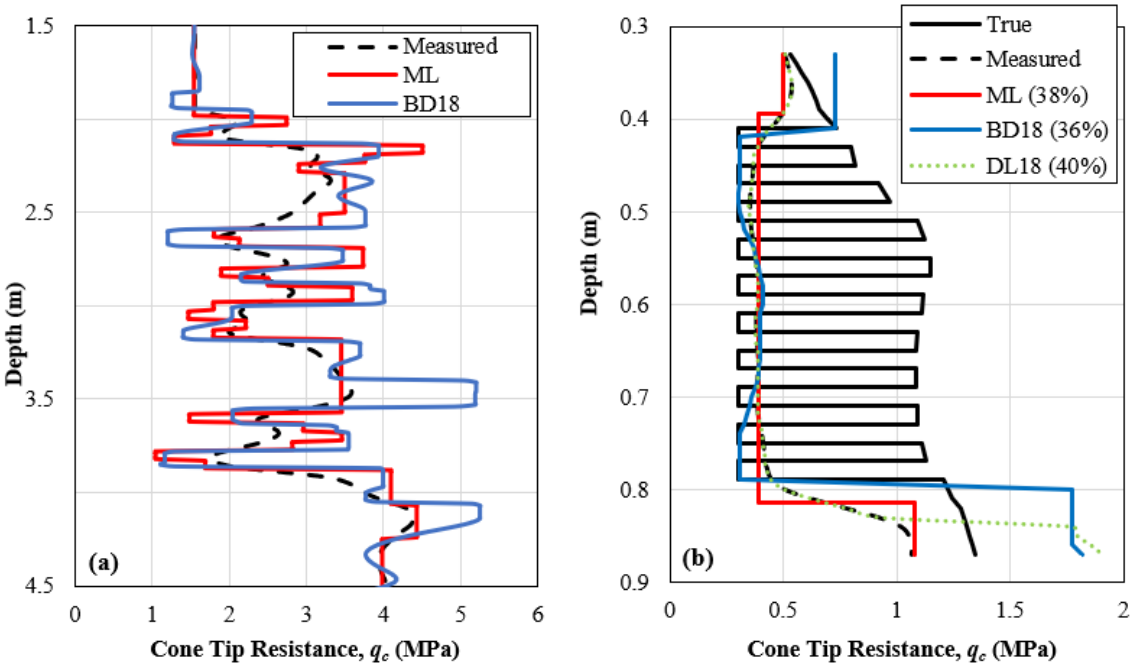


Figure 7. (a) Representative model corrections (BD18 vs. ML) on a CPT; (b) Model limitations when encountering very thin layers.

Additionally, although the test set was randomly sampled, any systematic bias in VCC simulations could propagate into both training and testing, potentially inflating model accuracy. Performance may also degrade in underrepresented parameter domains (e.g., $q^t/q^m < 0.3$ or > 6) or for different cone geometries and stress conditions. The model's reliability diminishes at CPT trace boundaries, where key features cannot be computed due to limited spatial context. While supervised learning was chosen for interpretability, unsupervised alternatives might exploit the information embedded in the CPT data more fully, but at the cost of transparency.

The model also cannot reliably resolve volume-averaging effects from intra-strata noise in layers thinner than ~1.1 H/d_c. Such limitations are demonstrated in Fig. 7(b) using a physical test with 1 cm interbeds (Van der Linden et al., 2018), where all models, including the ML model, perform poorly, and all three models have roughly the same MAPE.

CONCLUSION

This study developed and tested an ML model to correct CPT volume-averaging effects. The model outperformed existing solutions on test data to a statistically significant degree, with a mean absolute percentage error of 13%. Its limitations include: (i) reduced accuracy in very thin

© ASCE

layers and in conditions beyond the training set's parameter space; (ii) interpretability challenges typical of ML-based approaches; and (iii) uncertainties inherent to virtual methods' abilities to represent physical reality. Despite the limitations, the proposed ML model demonstrates the feasibility of a new data-driven approach to CPT inversion modeling. Its continued refinement depends on broader, higher-quality datasets. Virtual modeling remains essential to this process but must be rigorously validated against physical reality.

REFERENCES

Ahmadi, M. M., and Robertson, P. K. (2005). "Thin-layer effects on the CPT qc measurement. *Canadian Geotechnical Journal*, 42(5), 1302–1317.

Boulanger, R. W., and DeJong, J. T. (2018). "Inverse filtering procedure to correct cone penetration data for thin-layer and transition effects". In *Cone Penetration Testing 2018* (pg. 25-44). CRC Press, London.

Ciantia, M. O., Arroyo, M., Butlanska, J., and Gens, A. (2016). "DEM modelling of cone penetration tests in a double-porosity crushable granular material." *Computers and Geotechnics*, 73, 109-127.

Cooper, J., Martin, E. R., Yost, K. M., Yerro, A., and Green, R. A. (2022). "Robust identification and characterization of thin soil layers in cone penetration data by piecewise layer optimization." *Computers and Geotechnics*, 141, 104404.

De Greef, J., and Lengkeek, H. J. (2018). "Transition-and thin layer corrections for CPT based liquefaction analysis." In *Cone Penetration Testing 2018* (pp. 317-322). CRC Press, London.

Geyin, M., and Maurer, B. W. (2021). "Evaluation of a cone penetration test thin-layer correction procedure in the context of global liquefaction model performance." *Engineering Geology*, 291, 106221.

Geyin, M., Maurer, B. W., Bradley, B. A., Green, R. A., and van Ballegooy, S. (2021). "CPT-based liquefaction case histories compiled from three earthquakes in Canterbury, New Zealand." *Earthquake Spectra*, 37(4), 2920-2945.

Khosravi, A., Martinez, A., and DeJong, J. T. (2020). "Discrete element model (DEM) simulations of cone penetration test (CPT) measurements and soil classification." *Canadian Geotechnical Journal*, 57(9), 1369-1387.

Maurer, B. W., and Sanger, M. D. (2023). "Why "AI" models for predicting soil liquefaction have been ignored, plus some that shouldn't be." *Earthquake Spectra*, 39(3), 1883-1910.

Rateria, G., Geyin, M., and Maurer, B. (2024). *CPT-Based Liquefaction Case Histories from Global Earthquakes: A Digital Dataset*. DesignSafe-CI.

Robertson, P. K., and Wride, C. E. (1998). "Evaluating cyclic liquefaction potential using the cone penetration test." *Canadian geotechnical journal*, 35(3), 442-459.

Van Der Linden, T. I., De Lange, D. A., and Korff, M. (2018). "Cone penetration testing in thinly inter-layered soils." *Geotechnical Engineering*, 171(3), 215-231.

Yost, K. M., Green, R. A., Upadhyaya, S., Maurer, B. W., Yerro-Colom, A., Martin, E. R., and Cooper, J. (2021). "Assessment of the efficacies of correction procedures for multiple thin layer effects on Cone Penetration Tests." *Soil Dynamics and Earthquake Engineering*, 144, 106677.

Yost, K. M., Yerro, A., Green, R. A., Martin, E., and Cooper, J. (2022). "MPM modeling of cone penetrometer testing for multiple thin-layer effects in complex soil stratigraphy." *Journal of Geotechnical and Geoenvironmental Engineering*, 148(2), 04021189.

© ASCE

A Hybrid Physics-Guided and Machine-Learning Framework for Modeling Ground Subsidence in the Greater Houston Area

Yong Je Kim, Ph.D., A.M.ASCE[1]; Arip Syaripudin Nur, S.M.ASCE[2]; and Jinwoo An, Ph.D., A.M.ASCE[3]

[1]Assistant Professor, Dept. of Civil, Environmental, and Construction Engineering, Univ. of Texas at El Paso, El Paso, TX (corresponding author). Email: ykim14@utep.edu
[2]Graduate Student, Dept. of Civil and Environmental Engineering, Lamar Univ., Beaumont, TX. Email: anur@lamar.edu
[3]Assistant Professor, Dept. of Civil Engineering, Univ. of Texas Rio Grande Valley, Edinburg, TX. Email: jinwoo.an@utrgv.edu

ABSTRACT

Ground subsidence, primarily driven by excessive groundwater extraction, poses a serious threat to heavily urbanized regions worldwide, including the Greater Houston area (GHA). This study introduces a hybrid framework that integrates physics-based modeling and machine learning to deliver robust, regional-scale forecasts of ground subsidence. Our approach uniquely combines multi-temporal InSAR and GPS data with geological and hydrological records, enabling the identification of both direct and indirect controls on subsidence. The resulting susceptibility map, validated by robust metrics, provides actionable insights for infrastructure planning and risk mitigation. Notably, the susceptibility map extends beyond current observations by incorporating multiple environmental and anthropogenic factors, allowing for the prediction of future risk zones even where subsidence has not yet been observed. This work advances the field by demonstrating how data-driven susceptibility mapping can reveal emerging hazards and guide proactive management strategies. Our findings highlight the importance of factors such as lithology, land use, and proximity to rivers, in addition to groundwater extraction, in controlling subsidence susceptibility in the GHA.

INTRODUCTION

Ground subsidence, the gradual sinking of the Earth's surface due to the compaction of subsurface materials (Amelung et al. 1999), leads to irreversible consequences and long-term environmental and infrastructural impacts (Susilo et al. 2023). This phenomenon presents a significant, though often understated, threat to major urban centers globally, including the Greater Houston Area (GHA). While subsidence can result from natural processes such as sediment compaction, sinkhole formation, or tectonic activity (Nicholls et al. 2021; Sulapas et al. 2024), the most rapid and severe cases are typically anthropogenic. These are primarily driven by accelerated primary compaction associated with the extraction of subsurface fluids, particularly groundwater, oil, and gas (Wu et al. 2022).

The greater Houston area of Texas, including Harris, Galveston, Brazoria, Fort Bend, and Montgomery Counties, and surrounding counties (Figure 1), is ranked as the sixth-largest metropolitan area in the United States, with a population exceeding 7.8 million as of 2024 (census.gov). This region has experienced ground subsidence since the 1920s, primarily due to excessive groundwater extraction (Coplin and Galloway 1999). Evidence of subsidence has been

© ASCE

documented through various geodetic and remote sensing methods, including groundwater level monitoring, GPS networks, and satellite imagery analysis. Among the most effective tools for subsidence monitoring is interferometric synthetic aperture radar (InSAR). Using European Remote Sensing (ERS-1 and ERS-2) satellite data, Qu et al. (2015) reported subsidence rates reaching up to 53 mm/year between 1993 and 2000. Further analysis utilizing data from Envisat and the Advanced Land Observing Satellite (ALOS) revealed that subsidence rates exceeded 30 mm/year in the Houston-Galveston area between 2004 and 2011. Miller and Shirzaei (2019) employed Sentinel-1 data from 2015 to 2017 and ALOS data from 2007 to 2011, identifying maximum subsidence rates of 49 mm/year and 34 mm/year, respectively. Similarly, Khan et al. (2022) analyzed Sentinel-1 data from 2016 to 2020 and reported subsidence of up to 9 cm in certain areas. Liu et al. (2022) identified relatively stable zones within the Houston metropolitan area, attributing this stability to strict groundwater regulations in Area 1. In contrast, adjacent regions such as Katy and The Woodlands, where regulatory controls are more lenient, exhibited subsidence rates of at least 20 mm/year. These findings are corroborated by Nur et al. (2025) who demonstrated a strong correlation between elevated subsidence rates and accelerated groundwater extraction in regions with less stringent groundwater management policies.

Despite longstanding awareness of subsidence-related issues, reliably forecasting ground deformation in large metropolitan areas remains a formidable challenge due to limited subsurface information, variable climatic influences, and the complexity of local geophysical conditions. In this study, we present a hybrid physics-guided and machine learning framework that integrates multi-source geospatial and geotechnical data for subsidence prediction in the GHA. A key original contribution of this work is the demonstration that susceptibility mapping, which incorporates not only current deformation but also geological, hydrological, and anthropogenic factors, can identify areas at risk of future subsidence—even where significant deformation has not yet been observed. This approach enables proactive risk management and infrastructure planning. Furthermore, our analysis systematically assesses the relative importance of multiple factors, revealing that, in addition to groundwater extraction, variables such as lithology, land use/land cover, proximity to rivers, and topographic attributes play significant roles in determining subsidence susceptibility. This comprehensive, transferable methodology advances the field and provides a blueprint for other urban regions facing similar challenges.

MATERIALS AND METHODS

InSAR Data

In this study, we utilized Sentinel-1 radar imagery acquired between January 2020 and March 2023, processed using the Persistent Scatterer Interferometric Synthetic Aperture Radar (PS-InSAR) technique, specifically employing the Stanford Method for Persistent Scatterers (StaMPS) algorithm as outlined by Nur et al. (2024). Line-of-sight (LOS) deformation measurements from the Sentinel-1 time series were projected into the vertical direction using the methodology described in Nur et al. (2024). The resulting vertical displacement time series served as history-matching targets for the numerical model. Consistent with our previous research in the GHA, we excluded the horizontal component of deformation, as vertical motion is both the dominant displacement direction and most directly indicative of subsidence processes.

The InSAR analysis, conducted using the StaMPS method, yielded mean vertical deformation maps for the GHA, as presented in Figure 2. These maps use a color scale ranging

© ASCE

from blue to red to represent increasing rates of subsidence, with maximum rates reaching approximately 20 mm/year. As expected with the PS-InSAR technique—particularly the StaMPS implementation—a higher density of coherent measurement points is observed in urban areas, while vegetated and agricultural regions exhibit sparser data coverage due to lower signal coherence. Notable subsidence, with rates approaching 20 mm/year, was identified in several parts of the region, particularly in western communities such as Katy and northern suburbs including Spring and The Woodlands.

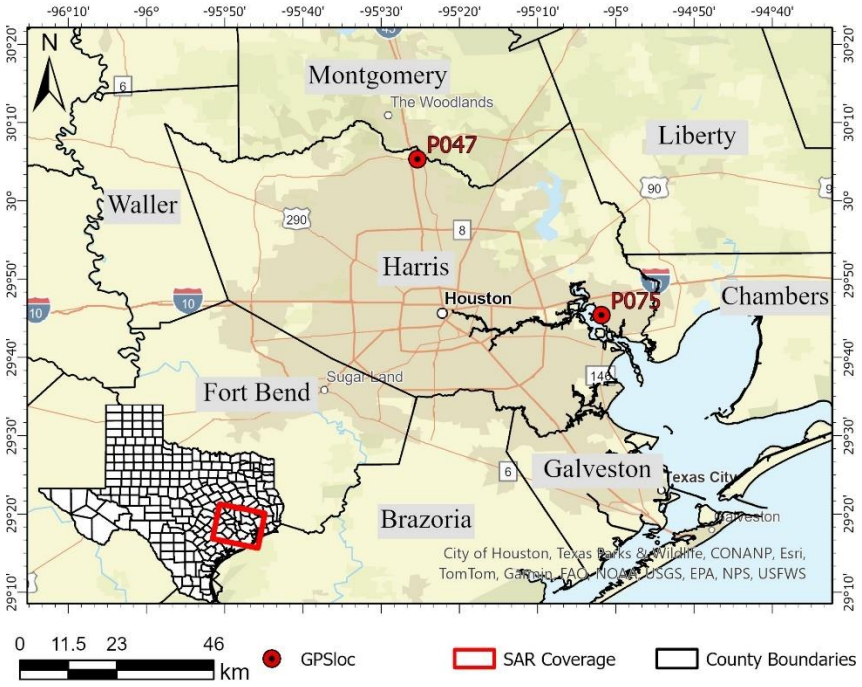


Figure 1. Map depicting the SAR coverage (red rectangle) and GPS stations within the greater Houston Area, Texas

Following the generation of the ground subsidence map, a total of 10,652 data points representing both subsiding and non-subsiding areas were selected for analysis. Of these, 5,326 points within identified subsidence zones were randomly sampled for modeling purposes. An equal number of points (5,326) were randomly selected from non-subsiding areas to ensure balanced class representation. To accurately distinguish between subsidence and non-subsidence, the average vertical ground deformation rate (in cm/year) was used as a classification threshold. Points with deformation rates below –0.3 cm/year were labeled as subsiding (coded as 1), while those with rates above this threshold were labeled as non-subsiding (coded as 0). This random sampling approach for binary classification is consistent with methodologies employed in prior studies (Alesheikh et al. 2024; Jafari et al. 2023; Zhang et al. 2023). For deep learning model development, the dataset was partitioned equally into training (50%) and testing (50%) subsets for both classes. The training datasets for subsidence and non-subsidence were merged to develop the ground subsidence susceptibility model, while the combined testing datasets were used to evaluate model performance (Hakim et al. 2020; Han et al. 2021; Nur et al. 2022).

© ASCE

Model Development and Evaluation

The framework for generating ground subsidence susceptibility maps using PS-InSAR, geographic information systems (GIS), and a deep learning algorithm is illustrated in Figure 3. The process begins with the acquisition of Sentinel-1 SAR images, which are preprocessed through co-registration and the generation of a single-reference interferogram using the two-pass interferometric technique. Subsequently, Persistent Scatterer processing is performed using the StaMPS algorithm, producing both a ground subsidence map and a time series of vertical deformation.

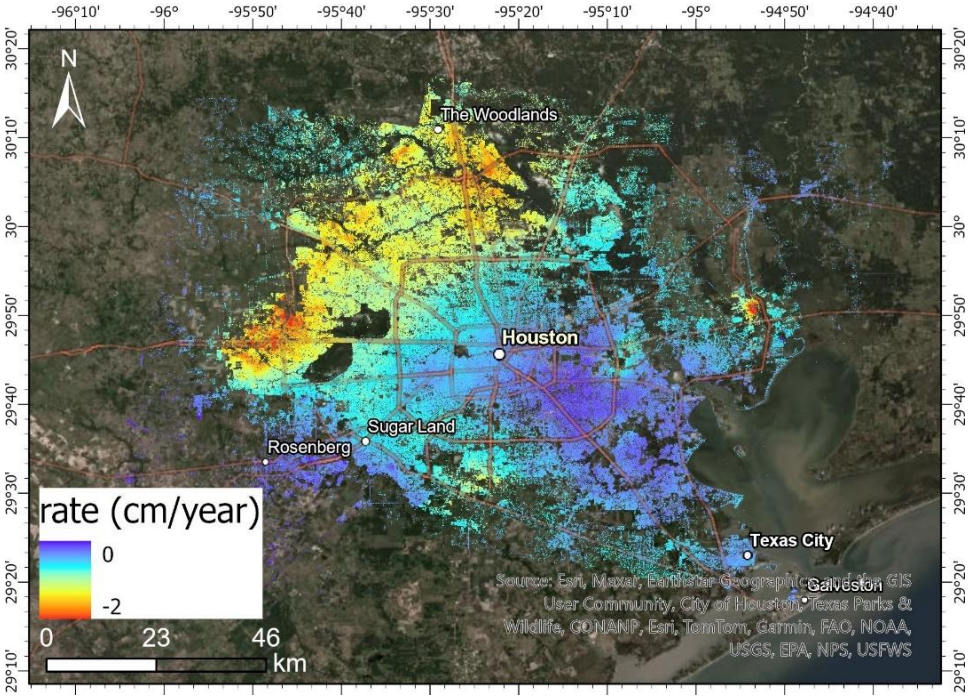


Figure 2. Vertical rate (displacement velocity) observation points derived from Nur et al., (2024) data from Sentinel-1.

A spatial database was constructed by collecting GIS-based environmental and anthropogenic factors associated with ground subsidence. Twelve conditioning factors—spanning geological, topographical, anthropogenic, and hydrological domains—were identified based on their relevance in prior studies (Bui et al. 2018; Choi et al. 2010; Ghorbanzadeh et al. 2018; Hakim et al. 2020, 2023; Lee et al. 2012; Oh et al. 2019; Pradhan et al. 2014; Ranjgar et al. 2021), as shown in Table 1. These variables were standardized using the quantile classification method. To ensure consistency across datasets, all raster layers were resampled to a common spatial resolution of 90 meters. Spatial correlation analysis, including multicollinearity checks and the frequency ratio method, was employed to evaluate the probabilistic relationship between subsidence occurrence and each class of the conditioning factors. The final stage involved the development and training of a Convolutional Neural Network (CNN) for ground subsidence susceptibility mapping. Model performance was assessed using the area under the receiver operating characteristic (AUROC) curve and root mean square error (RMSE) metrics.

© ASCE

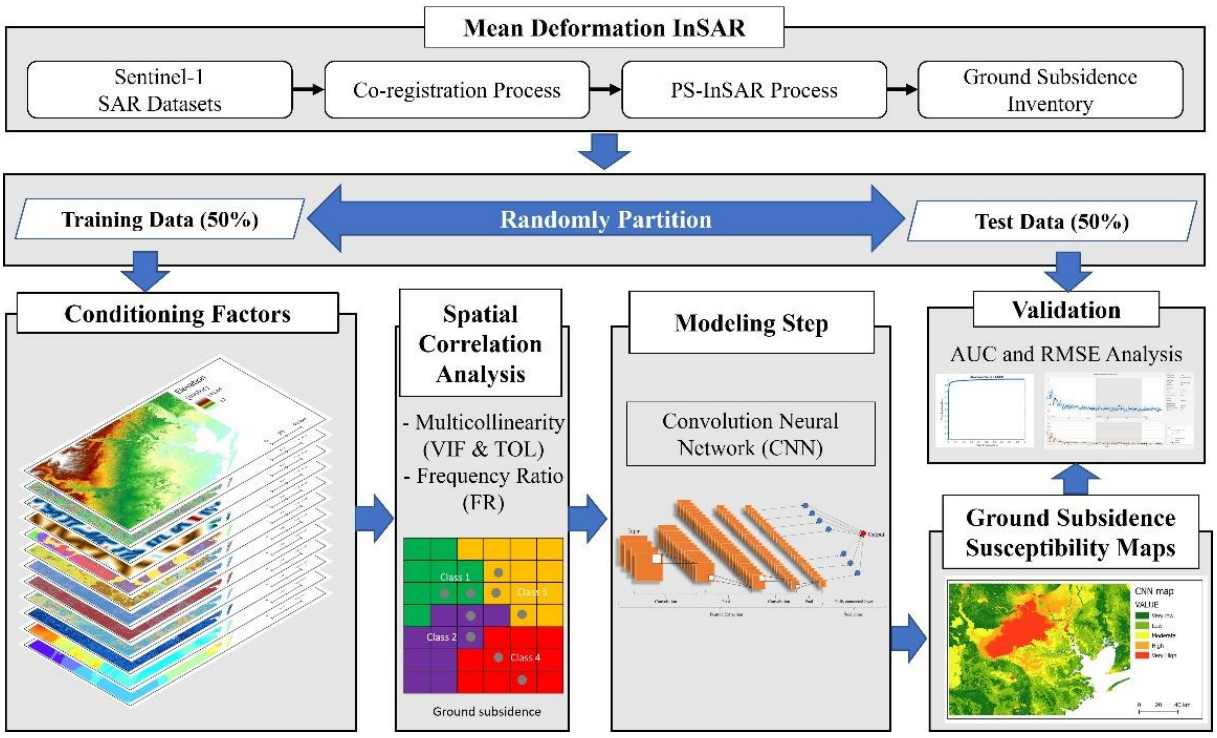


Figure 3. Methodological flow chart of the study.

RESULTS AND DISCUSSION

The findings of this study offer valuable insights into the spatial distribution and contributing factors of ground subsidence across the GHA. The high-resolution subsidence map derived from PS-InSAR analysis reveals significant spatial variability, highlighting the complex nature of subsidence in this urban environment. Notably, elevated subsidence rates were observed in the northern and western portions of the GHA—particularly in areas such as Spring, The Woodlands, and Katy—which is consistent with prior studies identifying these regions as centers of intensive groundwater extraction. This spatial variability in subsidence is likely influenced by localized differences in geological composition, aquifer characteristics, and patterns of groundwater withdrawal.

A key advantage of the susceptibility map (Figure 4) over the direct subsidence observation map (Figure 2) is its predictive capability: while the observation map reflects only current or past deformation, the susceptibility map integrates multiple conditioning factors (e.g., lithology, land use, proximity to rivers and roads, topography, and water level changes) to estimate the potential for future subsidence, even in areas where significant deformation has not yet been observed. This allows stakeholders to proactively identify and manage emerging risk zones, rather than reacting only to areas where subsidence is already occurring.

To evaluate the interrelationships among the conditioning factors used in the susceptibility model, a multicollinearity assessment was conducted (see Table 1). All variables exhibited Variance Inflation Factor (VIF) values below the commonly accepted threshold of 10 and tolerance (TOL) values above 0.1, indicating an absence of problematic multicollinearity. The highest VIF was recorded for water level altitude (2.60), while the lowest TOL was associated with lithology (0.46), with TOL values ranging between 0.38 and 1.00. These results confirm the

© ASCE

suitability of all selected factors for inclusion in the ground subsidence susceptibility model and support the robustness of the subsequent predictive analysis.

A ground subsidence susceptibility map was produced using 12 conditioning factors, training data extracted from the ground subsidence inventory map, and a Convolutional Neural Network (CNN) algorithm (Figure 4). Susceptibility indices were calculated for all pixels within the study area and subsequently reclassified into five susceptibility levels—very low, low, moderate, high, and very high—using the quantile classification method, following established approaches in previous studies (Han et al. 2021; Nur et al. 2022, 2023). The CNN model classified 26.59% of the area as very low susceptibility, 33.73% as low, 21.02% as moderate, 9.51% as high, and 9.15% as very high.

A strong spatial correlation was observed between the areas of significant subsidence identified in the mean vertical deformation map (Figure 2) and the regions classified as high and very high susceptibility in the generated susceptibility map (Figure 4). This alignment highlights the effectiveness of the model, which was trained on high-resolution subsidence inventory data, in accurately delineating zones prone to ground deformation. Areas categorized as moderate to very high susceptibility are considered at risk for future subsidence, while those labeled as very low or low are expected to remain relatively stable.

While groundwater extraction is the dominant driver of subsidence in the GHA, our analysis reveals that other factors—such as lithology, land use/land cover, proximity to rivers, and topographic attributes—also play significant roles in determining susceptibility. For example, areas with compressible clay-rich sediments, intensive urban development, or close proximity to major water bodies exhibit higher susceptibility, even when current groundwater extraction rates are moderate. This underscores the importance of a multi-factor approach for comprehensive risk assessment.

Table 1. Multicollinearity results.

Factors	Collinearity Statistics	
	Tolerance	**VIF**
Aspect	1.00	1.00
Distance to River	0.91	1.10
Distance to Road	0.81	1.24
Elevation	0.58	1.73
LULC	0.77	1.31
Lithology	0.46	2.17
Plan Curvature	0.73	1.37
Profile Curvature	0.74	1.35
Slope	0.82	1.22
TWI	0.76	1.31
Water Level Difference (2018-2023)	0.65	1.55
Water Level Altitude (2021)	0.38	2.60

Evaluating the accuracy and reliability of ground subsidence susceptibility models is a critical component of their development. In this study, model performance was assessed using the area under the receiver operating characteristic curve (AUROC) and the root mean square error (RMSE) metrics (Balogun et al. 2021; Nguyen et al. 2019). The CNN model yielded an

© ASCE

RMSE of 0.2459 during the testing phase, while the ROC analysis produced an AUROC of 0.9862. Since the AUROC value significantly exceeds the threshold of 0.5, the ground subsidence susceptibility map generated by the CNN algorithm is considered highly reliable for predicting high-risk subsidence zones within the GHA. This map serves as a valuable decision-support tool for urban planners and policymakers aiming to mitigate subsidence hazards.

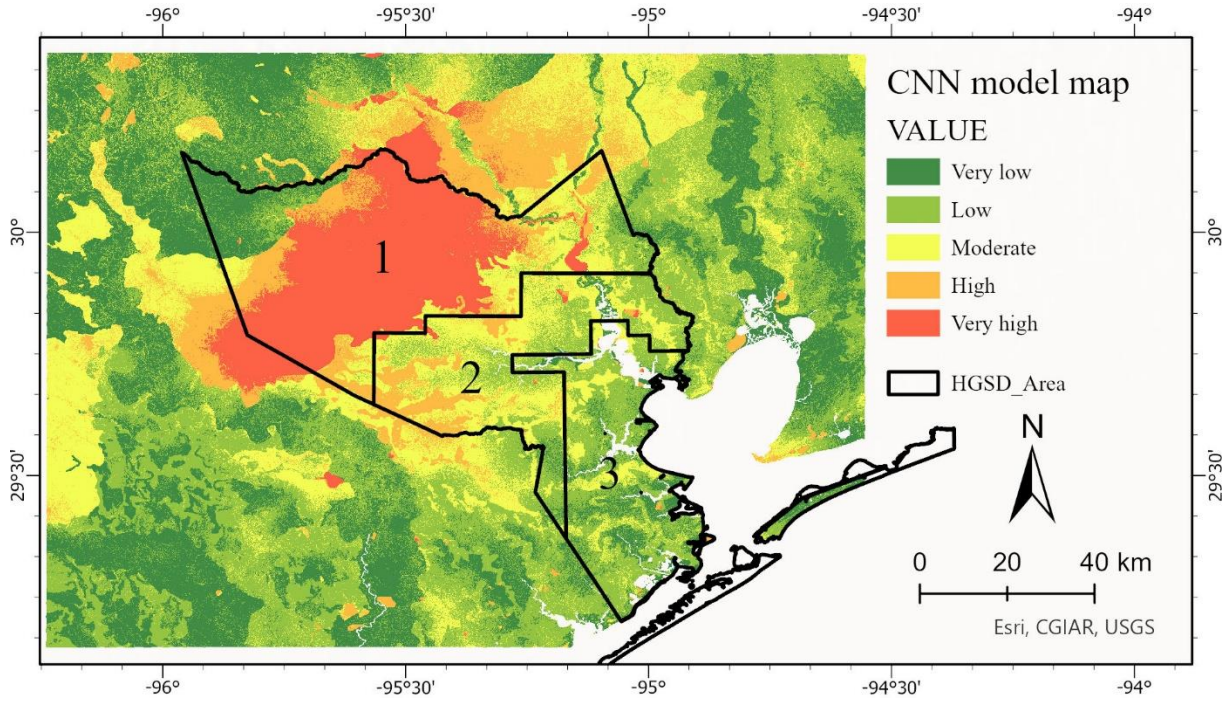


Figure 4. Ground subsidence susceptibility map of the study area.

To address subsidence mitigation, the Harris-Galveston Subsidence District (HGSD) has implemented a regulatory plan informed by groundwater and subsidence monitoring data, population and water demand projections, and coordination with regional alternative water providers. Figure 4 delineates the three regulatory areas under HGSD jurisdiction. While all areas share the common objective of reducing subsidence through overall groundwater withdrawal limits, each regulatory zone is subject to tailored reduction targets based on available alternative water sources, hydrogeological conditions, and groundwater demand. Specifically, Area 3 restricts groundwater use to no more than 10% of total water demand. In Area 2, the cap is set at 20%, with the option for permittees to operate under a Groundwater Reduction Plan (GRP) subject to specific conditions. Similarly, in Area 1, groundwater extraction is limited to 20% of total demand, with permittees under an approved GRP required to reduce groundwater use to 40% by 2025 and further to 20% by 2035. Given the GHA's robust economic growth and expanding suburban development, the HGSD regulatory framework requires periodic updates to accommodate increasing population pressures and evolving water management strategies.

CONCLUSION

This study highlights the efficacy of integrating advanced remote sensing techniques with machine learning algorithms to assess and predict ground subsidence in complex urban settings.

© ASCE

Our approach advances the understanding of subsidence dynamics in the Greater Houston Area (GHA) and offers a transferable framework for other subsidence-prone regions. The PS-InSAR analysis identified significant subsidence patterns with rates up to 2 centimeters per year, while the CNN-based susceptibility map demonstrated high predictive accuracy for areas at risk of future ground deformation. Moreover, coupling subsidence susceptibility with flood hazard mapping revealed zones of compounded risk, underscoring the need for comprehensive urban flood risk management that addresses both subsidence and traditional flooding threats. Ultimately, this research emphasizes the critical role of continuous monitoring and multidisciplinary assessment in managing subsidence, particularly in urban regions like the GHA, where geological, hydrological, and anthropogenic factors interact in complex ways. The findings provide a robust foundation for informed decision-making in urban planning, water resource management, and flood mitigation in subsidence-vulnerable environments.

REFERENCES

Alesheikh, A. A., Z. Chatrsimab, F. Rezaie, S. Lee, A. Jafari, and M. Panahi. 2024. "Land subsidence susceptibility mapping based on InSAR and a hybrid machine learning approach." *The Egyptian Journal of Remote Sensing and Space Sciences*, 27 (2): 255–267.

Amelung, F., D. L. Galloway, J. W. Bell, H. A. Zebker, and R. J. Laczniak. 1999. "Sensing the ups and downs of Las Vegas: InSAR reveals structural control of land subsidence and aquifer-system deformation." *Geology*, 27 (6): 483–486. GeoScienceWorld.

Balogun, A. L., F. Rezaie, Q. B. Pham, L. Gigović, S. Drobnjak, Y. A. Aina, M. Panahi, S. T. Yekeen, and S. Lee. 2021. "Spatial prediction of landslide susceptibility in western Serbia using hybrid support vector regression (SVR) with GWO, BAT and COA algorithms." *Geoscience Frontiers*, 12 (3).

Bui, D. T., H. Shahabi, A. Shirzadi, K. Chapi, B. Pradhan, W. Chen, K. Khosravi, M. Panahi, B. Bin Ahmad, and L. Saro. 2018. "Land subsidence susceptibility mapping in South Korea using machine learning algorithms." *Sensors (Switzerland)*, 18 (8).

Choi, J. K., K. D. Kim, S. Lee, and J. S. Won. 2010. "Application of a fuzzy operator to susceptibility estimations of coal mine subsidence in Taebaek City, Korea." *Environ Earth Sci*, 59 (5): 1009–1022.

Coplin, L. S., and D. Galloway. 1999. "Houston-Galveston, Texas." *Land* subsidence in the United States: US geological survey circular, 1182: 35–48. Citeseer.

Ghorbanzadeh, O., T. Blaschke, J. Aryal, and K. Gholaminia. 2018. "A new GIS-based technique using an adaptive neuro-fuzzy inference system for land subsidence susceptibility mapping." *J Spat Sci*, 1–17. Mapping Sciences Institute Australia.

Hakim, W., A. Achmad, and C.-W. Lee. 2020. "Land Subsidence Susceptibility Mapping in Jakarta Using Functional and Meta-Ensemble Machine Learning Algorithm Based on Time-Series InSAR Data." *Remote Sens (Basel)*, 12 (21): 3627.

Hakim, W. L., M. F. Fadhillah, S. Park, B. Pradhan, J.-S. Won, and C.-W. Lee. 2023. "InSAR time-series analysis and susceptibility mapping for land subsidence in Semarang, Indonesia using convolutional neural network and support vector regression." *Remote Sens Environ*, 287: 113453.

Han, J., A. Nur, M. Syifa, M. Ha, C.-W. Lee, and K.-Y. Lee. 2021. "Improvement of Earthquake Risk Awareness and Seismic Literacy of Korean Citizens through Earthquake Vulnerability Map from the 2017 Pohang Earthquake, South Korea." *Remote Sens (Basel)*, 13 (7): 1365.

© ASCE

Jafari, A., A. A. Alesheikh, F. Rezaie, M. Panahi, S. Shahsavar, M.-J. Lee, and S. Lee. 2023. "Enhancing a convolutional neural network model for land subsidence susceptibility mapping using hybrid meta-heuristic algorithms." *Int J Coal Geol*, 277: 104350.

Khan, S. D., O. C. A. Gadea, A. Tello Alvarado, and O. A. Tirmizi. 2022. "Surface Deformation Analysis of the Houston Area Using Time Series Interferometry and Emerging Hot Spot Analysis." *Remote Sensing* 2022, Vol. 14, Page 3831, 14 (15): 3831. Multidisciplinary Digital Publishing Institute.

Lee, S., I. Park, and J. K. Choi. 2012. "Spatial prediction of ground subsidence susceptibility using an artificial neural network." *Environ Manage*, 49 (2): 347–358.

Liu, Y., G. Wang, X. Yu, and K. Wang. 2022. "Sentinel-1 InSAR and GPS-Integrated Long-Term and Seasonal Subsidence Monitoring in Houston, Texas, USA." *Remote Sensing* 2022, Vol. 14, Page 6184, 14 (23): 6184. Multidisciplinary Digital Publishing Institute.

Miller, M. M., and M. Shirzaei. 2019. "Land subsidence in Houston correlated with flooding from Hurricane Harvey." *Remote Sens Environ*, 225: 368–378. Elsevier.

Nguyen, P. T., et al. 2019. "Development of a Novel Hybrid Intelligence Approach for Landslide Spatial Prediction." *Applied Sciences*, 9 (14): 2824.

Nicholls, R. J., D. Lincke, J. Hinkel, S. Brown, A. T. Vafeidis, B. Meyssignac, S. E. Hanson, J.-L. Merkens, and J. Fang. 2021. "A global analysis of subsidence, relative sea-level change and coastal flood exposure." *Nat Clim Chang*, 11 (4): 338–342.

Nur, A. S., Y. J. Kim, and C. W. Lee. 2022. "Creation of Wildfire Susceptibility Maps in Plumas National Forest Using InSAR Coherence, Deep Learning, and Metaheuristic Optimization Approaches." *Remote Sens (Basel)*, 14 (17). MDPI.

Nur, A. S., Y. J. Kim, J. Lee, and C.-W. Lee. 2023. "Spatial Prediction of Wildfire Susceptibility Using Hybrid Machine Learning Models Based on Support Vector Regression in Sydney, Australia." *Remote Sens (Basel)*, 15 (3): 760.

Nur, A. S., Y. J. Kim, B. H. Nam, K. Park, and J. An. 2025. "Subsidence characterization of karst sinkholes using satellite remote sensing: A Missouri case study." *Geomechanics and Engineering*, 41 (1): 151. Techno-Press.

Nur, A. S., B. H. Nam, S. Choi, and Y. J. Kim. 2024. "Monitoring of ground subsidence using PS-InSAR technique in the Southeast Texas (SETX) Region." *International Journal of Geo-Engineering*, 15 (1): 13.

Oh, H.-J., M. Syifa, C.-W. Lee, and S. Lee. 2019. "Land Subsidence Susceptibility Mapping Using Bayesian, Functional, and Meta-Ensemble Machine Learning Models." *Applied Sciences*, 9 (6): 1248. MDPI AG.

Pradhan, B., M. H. Abokharima, M. N. Jebur, and M. S. Tehrany. 2014. "Land subsidence susceptibility mapping at Kinta Valley (Malaysia) using the evidential belief function model in GIS." *Natural Hazards*, 73 (2): 1019–1042. Kluwer Academic Publishers.

Qu, F., Z. Lu, Q. Zhang, G. W. Bawden, J. W. Kim, C. Zhao, and W. Qu. 2015. "Mapping ground deformation over Houston–Galveston, Texas using multi-temporal InSAR." *Remote Sens Environ*, 169: 290–306. Elsevier.

Ranjgar, B., S. V. Razavi-Termeh, F. Foroughnia, A. Sadeghi-Niaraki, and D. Perissin. 2021. "Land Subsidence Susceptibility Mapping Using Persistent Scatterer SAR Interferometry Technique and Optimized Hybrid Machine Learning Algorithms." *Remote Sens (Basel)*, 13 (7): 1326.

© ASCE

Sulapas, J. J. S., A. A. B. Ybañez, K. M. M. Marasigan, J. M. B. M. Grageda, and A. M. F. A. Lagmay. 2024. “Ground subsidence in major Philippine metropolitan cities from 2014 to 2020.” *International Journal of Applied Earth Observation and Geoinformation*, 133: 104107.

Susilo, S., R. Salman, W. Hermawan, R. Widyaningrum, S. T. Wibowo, Y. A. Lumban-Gaol, I. Meilano, and S.-H. Yun. 2023. “GNSS land subsidence observations along the northern coastline of Java, Indonesia.” *Sci Data*, 10 (1): 421.

Wu, P., M. M. Wei, and S. D’Hondt. 2022. “Subsidence in Coastal Cities Throughout the World Observed by InSAR.” *Geophys Res Lett*, 49 (7).

Zhang, L., A. Arabameri, M. Santosh, and S. C. Pal. 2023. “Land subsidence susceptibility mapping: comparative assessment of the efficacy of the five models.” *Environmental Science and Pollution Research*, 30 (31): 77830–77849.

© ASCE